LATERAL-LINE-INSPIRED MEMS-ARRAY PRESSURE SENSING FOR PASSIVE UNDERWATER NAVIGATION

Vicente I. Fernandez vicentef@mit.edu
Stephen M. Hou shou@mit.edu
Franz S. Hover hover@mit.edu
Jeffrey H. Lang lang@mit.edu
Michael S. Triantafyllou mistetri@mit.edu

Massachusetts Institute of Technology
77 Massachusetts Avenue
Cambridge MA, 02139

July 3, 2007

Abstract

This paper presents work toward the development of a novel MEMS sensing technology for AUVs. The proposed lateral line-inspired sensor system is a high-density array of pressure sensors for measuring hydrodynamic disturbances. By measuring pressure variations on a vehicle surface, a dense pressure sensor array will allow the AUV to detect, classify, and locate nearby obstacles and optimize its motion in unsteady environments. This approach is very similar to the canal lateral line system found in all fish which allow them to function in dark or clouded environments.

In order to lay the groundwork for developing the MEMS sensor and interpreting the pressure distributions, the paper also presents experiments demonstrating the discrimination between cylindrical obstacles of round and square cross sections with an array of off-the-shelf pressure sensors. Test objects with 5.1 cm and 7.6 cm diameters passed stationary sensors at 0.5 m/s and 0.75 m/s and with 1.3 and 5.1 mm separation. Hand chosen features and features chosen through a Principal Component Analysis are used to discriminate between object shapes under a variety of conditions. A classification error rate of under 2% is achieved across all velocities, sizes, and separations. These results lead to requirements for the density, sensitivity, and frequency response of the MEMS sensors, which fall well in the MEMS domain.

[1]This publication is the result of research sponsored by The MIT Sea Grant College Program, under NOAA grant number NA06OAR4170019, project number R/RT-2/RCM-17.

The pressure sensor array proposed here consists of hundreds of MEMS pressure sensors with diameters near 1 mm spaced a few millimeters apart fabricated on etched silicon and Pyrex wafers; a fabrication process for producing the array is described. A strain-gauge pressure sensor is analyzed and shown to satisfy specifications as required by the results from the aforementioned experiments. The sensing element is a strain gauge mounted on a flexible diaphragm, which is a thin (20 μm) layer of silicon attached at the edges to a square silicon cavity 2000 μm wide on a side. A source voltage of 10 V produces a sensor with a sensitivity on the order of 1 $\mu\mathrm{V/Pa}$. Since the thermal noise voltage is near 0.7 μV, the pressure resolution of the sensors is on the order of 1 Pa.

1 Introduction

The blind Mexican cavefish (*Astyanax fasciatus*) is capable of forming a full three-dimensional map of its surroundings [1, 2] and moving in new environments at high speeds without collisions. This surprising feat is accomplished without the use of electric fields, relying instead primarily on its lateral line organ. All fish have this organ, though not all use it to extent of the blind cavefish [1]. Many other lateral-line-mediated behaviors in fish have been identified by biologists, including tracking prey by their wake [3] and recognizing nearby physical objects [2]. The lateral line organ has no equivalent in the modern world of underwater vehicles, though many vehicles would greatly benefit from some of its

abilities. Presented here is a series of experiments and a sensor design directed toward translating the abilities of the lateral line organ into a sensor for autonomous underwater vehicles (AUVs).

The basic sensory unit of the lateral line organ is the neuromast, which is a collection of drag-based flow velocity sensors. Neuromasts are used in two manners. First they are distributed on the surface of the fish protruding directly into the open water. In this arrangement, the neuromasts are directly stimulated by the local fluid velocity. Second, they are enclosed in canals that open to the outside flow periodically though pores [4]. These canals have been described as an array of pressure gradient sensors [5], since a difference in pressure between adjacent pores drives the fluid motion in the canal, stimulating the neuromasts. Through studies selectively deactivating the canals, it has been found that the imaging abilities of the lateral line appear to be predominantly accomplished by its canal system [1].

While an implementation identical to the lateral line organ is not practical, the information provided by the lateral line would greatly benefit AUVs. In particular, the ability to locate and obtain information about nearby obstructions is increasingly important as AUV's are finding applications in cluttered environments and surf zones. Also, the ability for flow mapping and identifying vortical structures allows the possibility for optimizing control and navigation in unsteady environments. In addition to these capabilities, a distributed pressure sensor would be completely passive and consequently require little power. The primary disadvantage would be its limited range.

Described here is the development of a sensor inspired by the canal system of the lateral line organ. This sensor attempts to directly extract information from the spatial pressure fields using an array of pressure sensors. This bypasses the pressure gradient to flow transformation of the canal system, considerably simplifying the design while possibly losing some favorable filtering characteristics [6]. The development of a full MEMS pressure sensor array, experiments with off-the-shelf sensors, and signal processing are subsequently considered in order to create a sensor system able to identify and classify nearby objects.

2 Experiments with Off-the-Shelf Sensors

This section describes experiments performed with off-the-shelf pressure sensors in order to investigate the differentiation of moving object shapes with the lateral line and to develop similar capabilities for a pressure sensor array. Two approaches are presented for distinguishing between two shapes of moving objects.

2.1 Background

Given the interesting abilities of the lateral line, there are many questions still being pursued on the sensory information it provides. The majority of the studies involving the lateral lines have focused on the response to a dipole stimulus, [5, 7, 8, 9, 10, 11, 12] which is used to model the oscillating tail of small prey. These studies have demonstrated that the lateral line is highly capable of locating dipole stimuli and discriminating between dipole frequencies and amplitudes.

A smaller number of studies have considered the lateral line's ability to investigate a fish's environment. In particular, blind cave fish have been found to detect and discriminate between stationary openings of different geometries [2, 13, 14]. Blind cave fish also detect wall boundaries to their environment through their lateral line [15, 16, 17]. In these scenarios, a blind fish must use the flow it generates to interrogate stationary objects.

The hydrodynamic stimuli from aquatic animals other than small prey has received the least attention. Larger fish, potentially predatory, are not well modeled by dipoles. Instead they are better approximated by blunt moving objects. Experiments by Vogel and Bleckmann [18] have demonstrated that goldfish use their lateral line to detect and discriminate the size, velocity and shape of passing rods in still water.

The purpose of the experiments with off-the-shelf components is to further investigate the amount of detail concerning a non-oscillatory stimulus that can be obtained through a pressure sensor array. The study concentrates on whether it is possible to tell the difference between cylinders with square and round cross-sections of various diameters. These stimuli are similar in basic structure and size, but the presence of sharp corners distinguishes the shape of the square. Similar to the earlier behavioral experiments by Vogel and Bleckmann, the objects are moved passed stationary sensors. The results will also provide information about the specifications necessary for constructing a dense MEMS pressure sensor array that can distinguish the details.

Off-the-shelf sensors are too large to pack densely in an approximation of the lateral line or the final MEMS array. However, since the stimuli in the experiments are moving at constant velocity, the time series from each

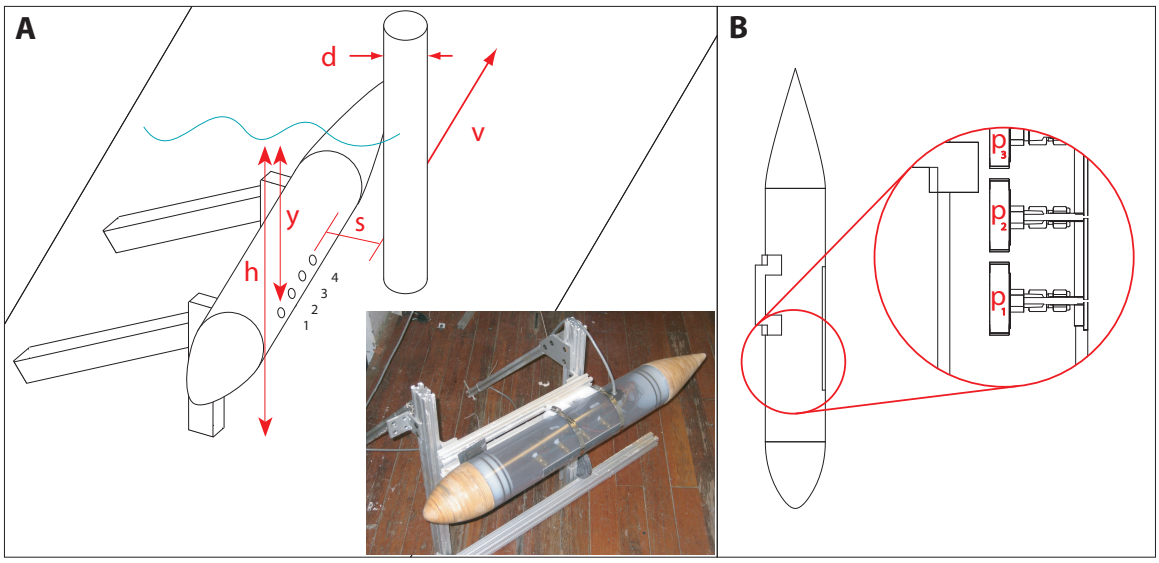

Figure 1: 1A: Schematic of experiments with cylindrical stimuli. The diagram depicts the housing with pressure ports along the side and a typical cylinder moving alongside. Several key quantities are labeled, including the separation between sensors and cylinder (s), the depth of the sensors (y), the total depth of the tank (h), the diameter of the cylinder (d), and the velocity of the cylinder (v). 1B: A close up of the pressure sensor and port geometry. The pressure sensors are labeled p_1 - p_3 in the cut-out view.

sensor can be used to approximate the spatial response sampled at intervals $d = V/f_s$, where V is the velocity of the stimulus and f_s is the temporal sampling frequency. This is an accurate approximation wherever the flow is steady from the frame of the moving stimulus. It does not hold well in the wake region of the cylinders, where, in addition to being turbulent, the presence and location of vortices is highly time dependent.

2.2 Experimental Procedure

Experiments were performed using gauge pressure sensors from Honeywell with a nominal sensitivity of 48 μV/Pa and response time of 1 μs. Four sensors are used in these experiments in a linear array. The redundancy between these sensors provides a sense of how valid any analysis is in the wake region. The four sensors were enclosed in a streamlined housing, as shown in Figure 1. They were connected to the outside flow through ports spaced 6.35 cm (2.5 in) apart. The sensor port geometry can be seen in Figure 1B. The sensors were connected to a rigid tube with a 0.472 cm (0.186 in) inner diameter. A small hole 1.3 mm (.050 in) in diameter and 3.2 mm (0.13 in) deep connected the tube to the outside. This layout was chosen to minimize the noise, given that it was not possible to flush mount the pressure sensors. The ports were positioned in a line in the region where the housing had a constant 11.4 cm (4.5 in) diameter.

The experiments were performed in the MIT Towing Tank. All of the experiments consisted of stationary sensors and moving stimuli. The specific arrangement can be seen in Figure 1A. The housing containing the sensors was fixed to a frame with the sensors facing horizontally. This frame was aligned with a movable carriage above the water and held in place with an array of weights. Vertical cylinders attached to the carriage were carried at constant velocity past the sensors. The motion of the cylinders began five meters from the sensors, reached its final velocity within 0.5 meters, and continued two meters past the sensors before stopping. Six seconds of pressure data were recorded at 2 kHz.

	5.1 mm Separation			
	7.62 cm Diameter		5.08 cm Diameter	
	0.50 m/s	0.75 m/s	0.50 m/s	0.75 m/s
Square	100 Runs	100 Runs	100 Runs	100 Runs
Round	100 Runs	100 Runs	100 Runs	100 Runs

Table 1: Table demonstrating the tests performed. Not included in the table are two sets of 100 runs (one for each cross section shape) at 0.75 m/s, 5.08 cm diameter, and 1.27 cm separation.

A number of variables were considered in the experiments. The difference between square and round cross sections was of primary interest, but it is also important to understand how sensitive the results are to carriage speed, cylinder diameter, and the separation from the

cylinder to the sensors. The orientation of the square cross section was kept constant, with the leading face perpendicular to the oncoming flow. Two sizes of the cross section were tested: 5.08 cm (2 in) and 7.62 cm (3 in). For the round cross section, the size refers to the diameter, and for the square cross sections it refers to the side length, so that the round cross section inscribes the square cross section. The two carriage velocities tested were 0.50 m/s and 0.75 m/s. Most of the tests were performed at a separation of 0.51 cm (0.2 in), but two sets were also taken at a larger separation of 1.27 cm (0.5 in). Ten sets of experiments were run with different combinations of these variables (Table 1). Each set consisted of one hundred passes of the cylinder past the sensors.

Calibration of the sensors was done immediately after testing without removing the setup from the water. This was necessary due to the sensitivity of the sensors to air bubbles. In order to calibrate all of the sensors at the same time and in place, a wave machine was used to generate waves in one end of the tank at approximately 1.5 Hz. The amplitude of the waves was measured at the position of the sensors while the pressure oscillations from the waves were recorded. After also recording the distance from the sensors to both the bottom of the tank and the water surface, the calibration was found using linearized surface wave theory [19], in which

$$A_p = \rho g \frac{\cosh\left[k\left(y+h\right)\right]}{\cosh\left[kh\right]} \cdot A_w \qquad (1)$$

determines the amplitude A_p of the pressure oscillation a distance y below the surface in water of depth h when the wave amplitude A_w is measured. In the equation, ρ is the density of water, g is the gravitational acceleration, and k is the wave number. The wavenumber of the surface waves is calculated from the dispersion relation $w^2 = gk\tanh\left[kh\right]$, where the frequency w is calculated by fitting a sine to the recorded pressure.

The cylinder testing plan is an accurate model of a vehicle or fish in an environment where the moving objects are at a Reynolds number of $2 \cdot 10^4$ to $6 \cdot 10^4$ and where the ratio of the separation between sensors and object (labeled s in Figure 1A) to the object radius is between 0.1 and 0.5. These conditions and geometry are relevant for fish in their exploration of new environments [13] and to vehicle operation in cluttered environments.

2.3 Results

In the results and analysis shown here, the raw data were initially processed as follows. First the hydrostatic pressure, found as the pressure before the cylinder approached, was removed by subtraction from the data of each sensor in each run. All pressure quantities in the figures and in text are therefore pressure differences with respect to the hydrostatic pressure. Second, some of the data has been resampled at a slower rate. The purpose of the experiments is to compare the spatial pressure distribution. The cylinder stimuli were run at two velocities (0.5 m/s and 0.75 m/s) past the sensors, but the data was collected at 2 kHz in all cases. This means that, after transforming the time histories with the velocities, the slower tests were sampled more closely in space. To remedy this, the slow tests were downsampled by a factor of 3/2. The final necessary transformation relates to the alignment. Each pressure trace was aligned by the point at which pressure crosses zero (with negative slope) near the leading edge of the stimulus. As can be seen from Figure 2, this feature is prominent and easy to identify. The steep slope at that point minimizes the variance due to noise. This point of alignment does not correspond to the same physical location of the stimulus in all cases. Experiments using an external trigger as well as potential flow simulations showed that the zero crossing occurred earlier for square cross sections than the round cross sections. However, looking forward to the use of the MEMS pressure array, an external verification of the position of a cylinder will not be available and the zero crossing makes a very good replacement.

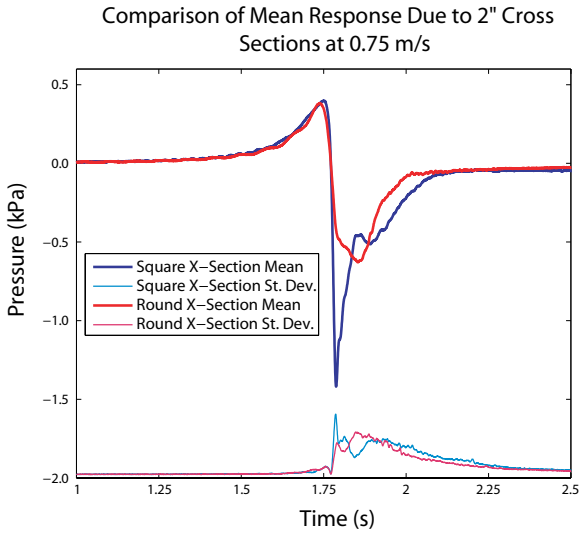

Figure 2: The results from two sets of tests comparing the pressure traces from different cross sections. Both cross sections had a diameter of two inches, velocity of 0.75 m/s, and separation of 0.51 cm (0.2 in). The means of each set of 100 runs is shown. The corresponding standard deviation is offset by -2000 Pa but on the same scale as the mean pressure traces.

The pressure traces resulting in all experiments had some basic similarities. Figure 2 gives the mean pres-

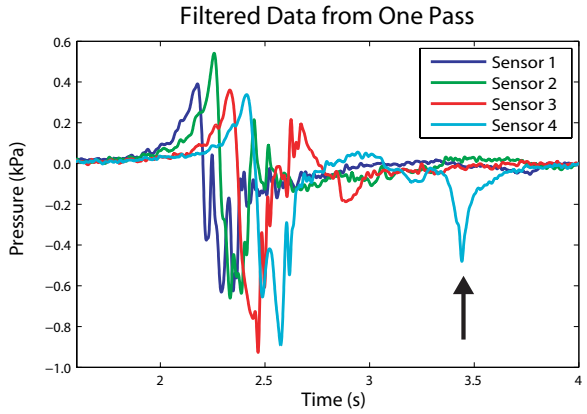

Figure 3: Pressure traces for a single run are depicted, filtered with a cut-off frequency of 100 Hz but not aligned. The low pressure spike marked with an arrow has the signature of a vortex impinging on the sensor port.

sure traces for both cylinder cross sections with two inch diameters and at 0.75 m/s. In all cases the pressure response to a passing cylinder could be described as a slow near-exponential rise in pressure ahead of the cylinder, followed by a sharp transition to negative pressure and a recovery back to the hydrostatic pressure. Due to the nature of the flow, there is a large amount of variance between runs even under the same conditions. This variance is not evenly distributed however. For the two examples shown in Figure 2, the standard deviation is also plotted. There is little deviation from the mean of 100 runs in each case until the sharp transition to negative pressure occurs. From that point on, there is a large amount of variation which trails off slowly. Qualitatively, much of this variance seems to stem from the unpredictable nature of the wake and the presence of vortices. Vortices show up in the wake as isolated, pointed, intrusions of low pressure (Figure 3). Although they are being shed regularly at a known frequency, the vortices are located at random in the pressure traces if at all. The initial phase of the vortex shedding determines whether a vortex is shed near one of the stationary sensors.

The three variables systematically tested were the cylinder size, velocity, and shape. The mean pressure traces for each variable are shown in Figures 4-6. In each case, the mean pressure trace is found across all sensors.

In comparing the results from the different sized cylinders (Figure 4), there is little change in the overall amplitude of the pressure traces. There is, however, a consistent increase in the length of time between the zero crossing at the leading edge and when the pressure recovers to the hydrostatic pressure. While this change

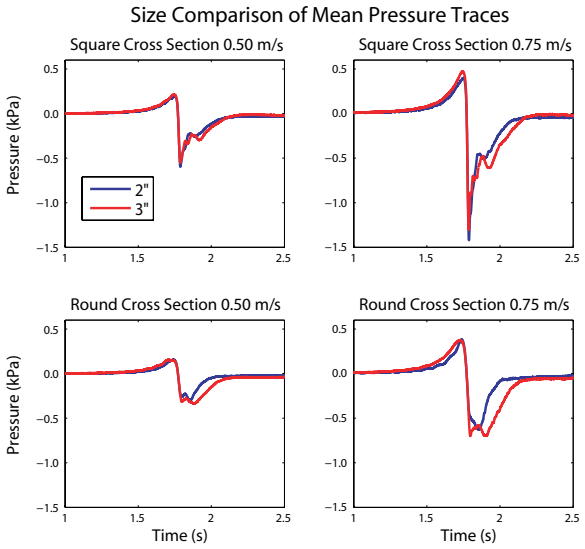

Figure 4: Plotted are the means of eight data sets, paired in order to compare the effects of the cylinder size. Each data set is composed of 100 runs.

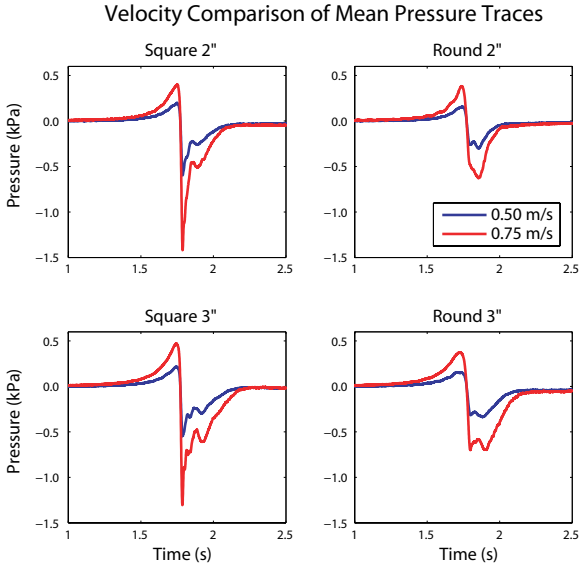

Figure 5: Plotted are the means of eight data sets, paired in order to compare the effects of the cylinder velocity. Each data set is composed of 100 runs.

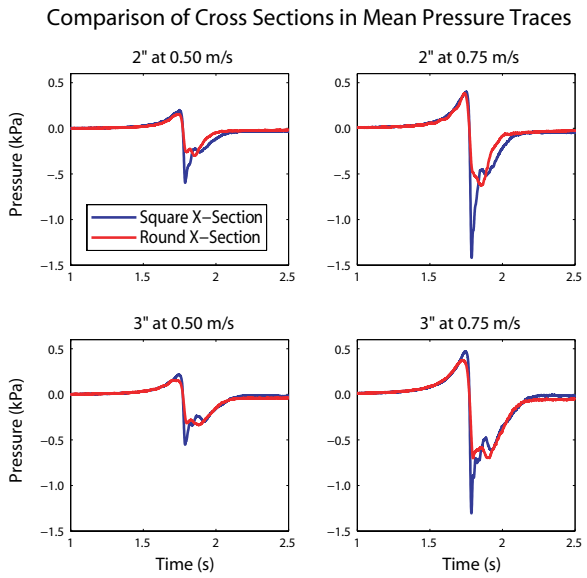

Figure 6: Plotted are the means of eight data sets, paired in order to compare the effects of the cylinder shape. Each data set is composed of 100 runs.

is evident in the mean pressure traces, it is much more difficult to pick out of individual pressure responses due to the large variability in that region.

A cylinder moving at a higher velocity creates a larger amplitude pressure response. This evident in Figure 5 and is expected from potential flow. A potential flow model of a circular cylinder in an infinite steady flow shows that the pressure behaves as

$$P - P_\infty = U^2 \cdot C(\bar{x}, r, \rho). \tag{2}$$

where U is the velocity of the cylinder, $\bar{x}$ is the position vector from the center of the cylinder, r is the radius of the cylinder, and ρ is the density of water [19]. The potential flow model is not a good one in this situation since it is based on a round cross section and cannot take into account the wake region. Despite this, it turns out to be surprisingly accurate. Given the velocities tested here, the model would imply that the pressure at 0.75 m/s is $\frac{9}{4}$ (2.25) larger than the pressure trace at 0.50 m/s. The scale factors were found to be 2.09, 2.12, 2.13, and 2.15 in clockwise order according to Figure 5. These scale factors minimize the difference squared between the trace at 0.75 m/s and the scaled 0.50 m/s trace. There does not seem to be any dependence on the shape or size for this effect. The scaling effect of velocity is particularly convenient because it is also possible to accurately determine the velocity of the stimulus by comparing the time lag between sensors. The effects of velocity can therefore be immediately removed.

Finally, the different cylinder cross section shapes are compared in Figure 6. Qualitatively, there are a number of apparent differences between the mean traces. The most striking is that the square cross section is characterized by a sharp negative peak of pressure immediately after the zero cross point, whereas this sharp peak is completely absent in for the round cross section. This is true for all the sizes and velocities tests. On the other hand, other differences seem dependent on the size of the cylinders. In particular, at the smaller diameter there seems to be a difference in the length of the wake which is not present at the higher speed. Also, the initial peak before the zero crossing point seems larger and sharper for the square cross sections at 0.75 m/s, but there is little difference with the round cross section at the lower velocity.

2.4 Analysis and Discussion

The goal of the analysis is to obtain a reliable approach to classify the cross-sectional shape of the cylinder stimulus from the pressure signature of a single pass. Preferably, the classification will be insensitive to velocity, size, and separation, at least those tested here. Also, the classification is ideally simple to apply to new pressure traces in order to classify them. All of the results described above are used as a training set in order to obtain a useful classification scheme. The question of locating the disturbance from background noise in order to perform the classification is not considered.

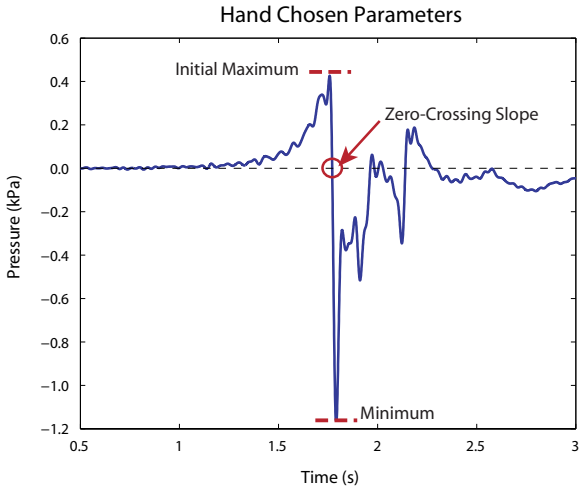

Figure 7: Diagram of hand chosen features. The three features initially chosen for analysis are marked on a sample pressure trace. The pressure data has been filtered with a cutoff frequency of 60 Hz.

2.4.1 Intuitive Features

The simplest approach to classification is to use intuition from the qualitative analysis of the mean pressure traces to select features. In this way the maximum before the zero crossing point (Max), the minimum immediately following the zero crossing point (Min), and the slope at the zero crossing point ($Slope$) were chosen as features (Figure 7). The slope at the zero crossing point was found by first filtering the data with a cutoff frequency of 60 Hz. The length of the wake region was not chosen as a feature, despite the fact that it was identified as a possible difference between pressure responses to different cross sections. This was due to its high variability and difficulty in quantifying for individual runs.

The relationship between the three chosen features and the cross sections of the cylinders is fairly complicated. At the same time, the features are heavily correlated. For example, the increase in amplitude that occurs from increasing the velocity of a cylinder would increase the magnitude of all three features. In order to remove some of this correlation, the three features were combined into two non-dimensional quantities. The first of these is a ratio of the minimum after the zero crossing to the maximum before the zero crossing: $\frac{Min}{Max}$. For the second, the slope at the zero crossing is made non-dimensional by the peak-to-trough change in pressure and unit time: $\frac{Slope}{Max-Min}$. These non-dimensional features have been calculated for every sensor in every run and plotted in Figure 8.

The intuitively chosen features separate the four thousand points into two adjacent clouds corresponding to the two cross sections tested in the experiments. Unfortunately the two clouds are not completely separable. For simplicity, a linear classifier was used such that all points on one side of the decision line are considered to be square and those on the other side to be round (Figure 8). The classifier was chosen to minimize the sum of squared errors, where the error for a single run is the difference between a desired distance from the line and the actual perpendicular distance to the line. The key is that the desired distance be positive for one class of objects in the training set and negative for the other class. The magnitude of the desired distance was arbitrarily set to one. The decision line is then found from

$$\bar{w} = \left(X^T X\right)^{-1} X^T \bar{y} \tag{3}$$

in which $\bar{w}$ is a vector of weights that define the decision boundary by $\bar{w} \cdot \bar{x} = 0$; X is a matrix made from the features such that each column corresponds to one feature and each row to one test; the vector $\bar{y}$ is the set of desired distances, with elements of ± 1 corresponding to the class of corresponding test. See [20] for details

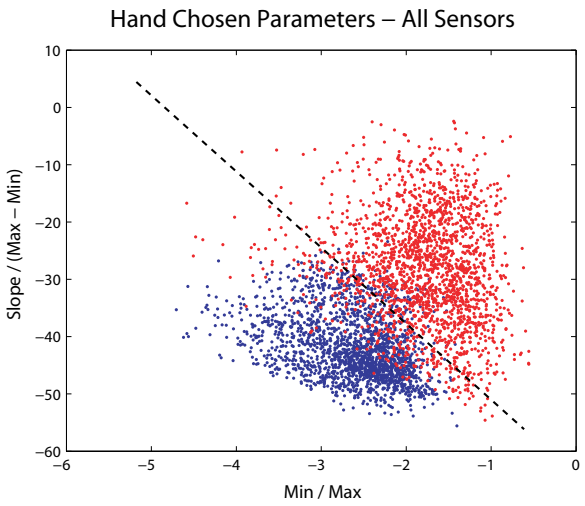

Figure 8: Scatterplot of individual traces according to their intuitively chosen features. All blue dots correspond to runs with square cross sections and red dots to those with round cross sections. All velocities, sizes, and separations are included. The decision line based on a sum of squared error criteria is marked as a dotted black line.

and a derivation. Minimizing the sum of squared errors makes it possible to obtain a classifier on a set that is not separable without knowing the probability distributions of the features for each class. The percentage of misclassified runs, shown in Figure 9, gives an estimate of the probability of error in the classifier. In addition, Figure 9 gives an idea of the distribution of the runs with respect to the classifier.

The primary advantage of these hand-chosen features is that they are very straightforward to find. Given a new time series or spatial distribution of pressure, the zero crossing point is distinctive and the features follow directly from it. This classification approach is also fairly impervious to different sampling rates, as long as they are high enough to estimate the slope well at the zero crossing point. The difficulty with this approach is that there is a fairly large misclassification rate (9.8%). As a result, one is left with the question of whether there are better features on which to base the classification.

2.4.2 Principal Component Analysis

A different approach to obtaining features is provided by Principal Component Analysis (PCA) [20, 21, 22]. This technique, closely related to the Karhunen-Loeve transform and singular value decomposition, obtains optimal features under specific conditions. The features are linear combinations of the pressure traces with coefficients

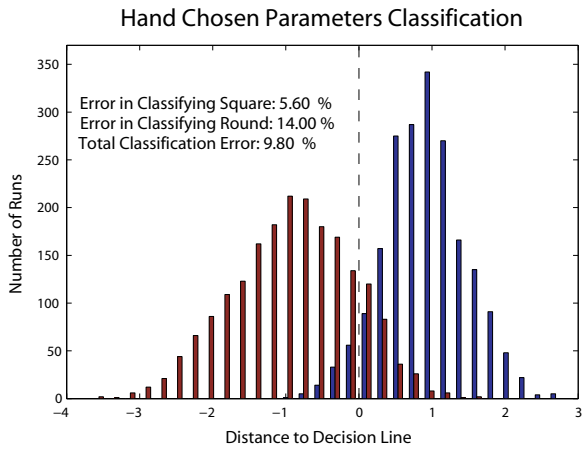

Figure 9: Histogram of the distance from the decision line marked in Figure 8. The blue histogram corresponds to the data from square cross sections and the red for data from round cross sections.

that are determined by PCA. The resulting features can in turn be analyzed in a similar manner to the hand chosen features in order to classify the cross sections of the cylinder stimuli.

Principal Component Analysis interprets each pressure trace (from a single run on a single sensor) to be a collection of highly correlated features. Each sample is considered to be a feature. Since there is data from multiple runs, once they are aligned, there are multiple observations of each feature. The purpose of PCA is to compress the data so that a small number of linear combinations of the original features (individual samples) best represent the entire set of data. These new features, which are linear combinations of the sampled points in a pressure trace, are the principal components. They are found so that each principal component has the maximum possible variance, subject to having unit area, and being uncorrelated with all the previous principal components. Implicit in this procedure is the assumption that the information of interest in the data set is that which has the largest variance. For example, it assumes that the difference in pressure traces generated by the different cross sections is larger than the variance in the data due to noise or turbulence. If this is not the case, the analysis would provide a compact representation of the noise. The uncorrelatedness constraint in the principal components is ideal for feature generation, since it removes the redundancy. The variance of the principal components typically drops off steeply, so that the data are well represented by considering only the first several components.

In implementation, PCA works as a singular value decomposition of the sample covariance matrix of the data ([21, 22]). One important detail in the implementation is that the mean of each initial feature (a sample point in the pressure trace) must be removed. This mean is take across all of the training data, not over each class. With the means removed, the sample covariance is straightforward to calculate.

Several PCAs were performed on the pressure traces. As mentioned, PCA does not optimize the features for classification. Ideally, the majority of the variation in the data would be due exclusively to the cross section shape. In that case, a Principal Component Analysis would produce features well suited for classifying the data by stimulus shape. Unfortunately this is not the case. In particular, the variation in the data due to velocity (Figure 5) is large in comparison to the variation from cross section shape. Therefore it was necessary to normalize each pressure trace by the maximum pressure before the zero crossing. This effectively removes the variance from velocity. Also, the differences in the responses of the sensors are enough to degrade the classification ability of a PCA in the same way. These differences between pressure sensors may be from variation in the calibration or in the transfer functions from the ports connecting them to the flow. As a result, the Principal Component Analysis which achieves the best classification uses a training set of normalized pressure traces from one sensor.

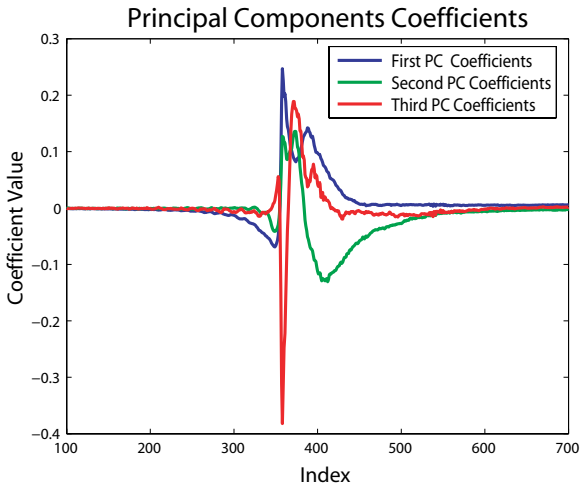

Figure 10: Coefficients for the first three principal components derived from the normalized of sensor 2. These are the coefficients for the linear combinations to generate the first three principal components. Data from all of the experiments were used in the PCA, but only from one sensor.

The coefficients for the first three principal components are plotted in Figure 10, ordered by largest variance. Examining these coefficients reveals information

about the features identified through PCA. For example, the coefficients for the first principal component are dominated by the region just after the zero crossing. Since the data was normalized by the maximum before the zero crossing point, one could argue that the first principal component is similar to the hand chosen $\frac{min}{max}$. However, the principal components are considerably more complex than the hand chosen features, since they contain contributions from all parts of the pressure trace including the wake. This leads to one of the difficulties with the Principal Component Analysis, which is that it is difficult to interpret the principal components.

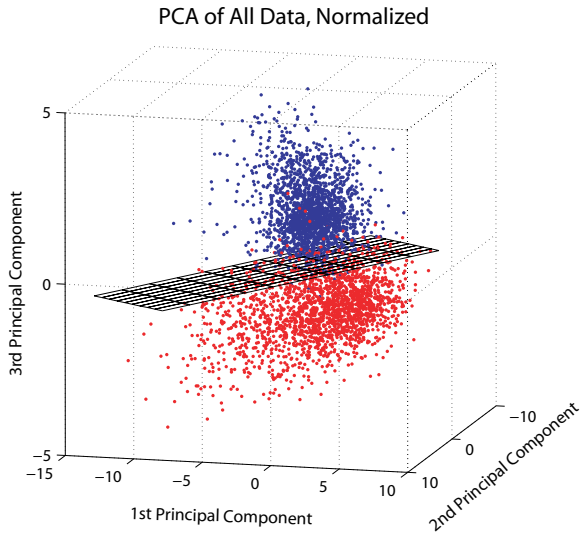

Figure 11: Scatterplot of data from all tests and sensors according to principal components. The coefficients for the principal components were found using data from only one sensor. In blue are the pressure traces corresponding to a square cross section and in red are those corresponding to a round cross section. The black plane bisecting the figure is the decision plane minimizing the sum of squared errors.

Interpreting the coefficients however is not necessary for classifying the pressure traces. Using the first three principal components, the data is divided into the two classes of interest (Figure 11). At this point, the principal components that were found using the data from only one sensor are being applied to all of the data. In addition to separating the shapes of the stimuli, the principal components are not strongly dependent on the other variables such as size and velocity. This is evident from the scatterplot of the data. The only data clouds formed correspond to the two shapes and these clouds are roughly ellipsoidal in form. There are also no dense clusters in the clouds that would correspond to differences in the other variables. In the same manner as before, a decision plane minimizing the sum of the squared error can be found, and the estimated probability of misclassification can be calculated (Figure 12). Using a Principal Component Analysis to obtain features, the misclassification rate is 1.2%, which is considerably better than the 9.8% rate obtained with the hand chosen features.

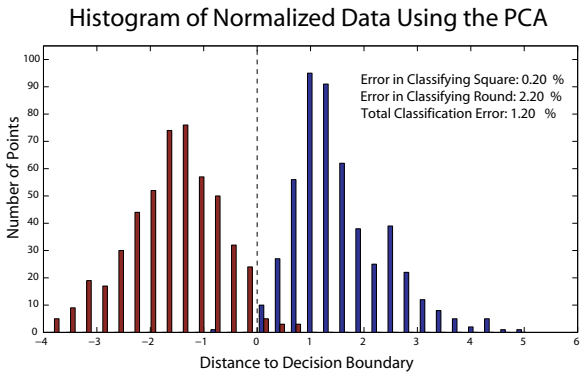

Figure 12: Histogram of the distance from the decision plane as shown in Figure 11. In blue is the data from the square cross section and in red from the round cross section.

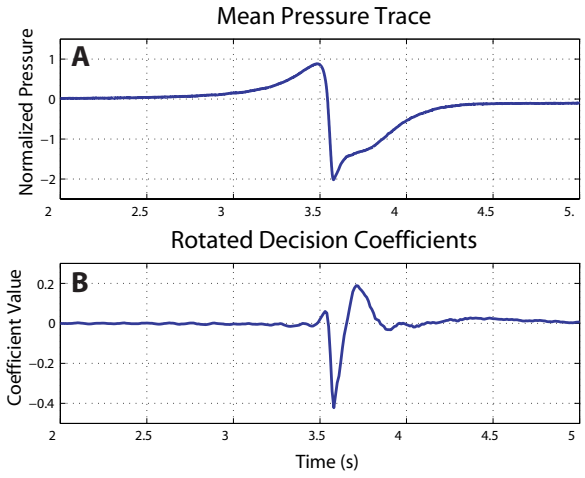

Figure 13: A: The mean pressure trace of sensor 2 from all experiments. This mean needs to be subtracted from any new data before trying to classify it with the results of the PCA. B: The coefficients for classifying a new pressure trace. These coefficients are the result of rotating the coordinates in Figure 11 so that one axis is normal to the decision plane.

2.4.3 Comparison

Features from Principal Component Analysis do a considerably better job in recognizing the different cross-sectional shapes than the hand chosen parameters. Unfortunately, it is more difficult to implement classification with principal components. With the hand-chosen

features, classification involves locating three points in the pressure response. For one of those points, the slope is calculated, but the others are just the pressure at the points. With this information, the classification of a new pressure trace can be made based on the sign of the distance d, defined by

$$d = w_2 \cdot \left(\frac{Min}{Max}\right)_{new} + w_1 \cdot \left(\frac{Slope}{Max - Min}\right)_{new} + w_0 \quad (4)$$

where the constants w_2, w_1, and w_0 come from the equation of the decision line in Figure 8, which is $w_2 \cdot \frac{Min}{Max} + w_1 \cdot \frac{Slope}{Max-Min} + w_0 = 0$. The distance will be positive for square cross sections and negative for round cross sections.

In the case of the principal components, there are essentially three steps for classifying a new pressure trace. First the zero crossing point must be located, just as in the other case. Second, the same mean pressure trace that was subtracted from all the data in the analysis (Figure 13B) must be removed from the new trace. With that, the distance to the decision plane can be found through a linear combination with the coefficients shown in Figure 13B. These coefficients are a combination of those for the principal components, rotated such that they form a coordinate normal to the decision plane. Thus only one linear combination is performed with the new data, and the result is compared to the intersection of the decision plane on that axis. Besides the added complexity, the fact that the mean from the training data must be subtracted before classification may limit the extent to which this procedure may be generalized.

3 MEMS Pressure Sensor Array Development

The experience gained from classifying cross sections as discussed earlier provides estimates of the requirements for a MEMS sensor array that can support the same classification. In particular the classification approach with hand chosen features lends itself simply to this task. The strictest constraint imposed on the spacing is in accurately obtaining the slope at the zero crossing point. In the initial analysis, the data was filtered with a cutoff frequency of 60 Hz. Combined with the velocity of the stimulus, this gives an equivalent spacing of 1.25 cm between samples. The other two measurements give a sense of the range of pressure necessary. The smallest peak pressure was approximately 200 Pa, while the largest pressure difference recorded was approximately 2 kPa. In order to locate the maximum and minimum, finer resolution than 200 Pa is needed, at least on the order of 20 Pa. The root-mean-square amplitude of the noise, including all sensor and electronics, was typically also approximately 20 Pa. These specifications are particular to the conditions of the experiments and therefore only provide a rough picture of the requirements.

The pressure sensor array proposed here consists of hundreds of MEMS pressure sensors with diameters near 1 mm spaced a few millimeters apart fabricated on etched silicon and Pyrex wafers; the sensors are arranged over a surface in various configurations, such as a single line, a patch consisting of several parallel lines (as shown in Figure 14), or specialized forms to fit the hull shape of a vehicle or its fins.

3.1 Membrane Design

The key feature of the sensor is a flexible diaphragm, which is a thin (20 μm) layer of silicon attached at the edges to a silicon cavity. A strain gauge consisting of four long and thin snaking resistors sits on the surface of the diaphragm. As the difference in pressure above and below the diaphragm changes, the diaphragm bends and the strain gauge resistances change. The four resistors are optimally designed and connected in a Wheatstone bridge configuration to maximize the pressure sensitivity. A schematic side view of one sensor is shown in Figure 15. These design requirements are within the scope of MEMS technology.

3.2 Stress, Strain, and Pressure

To express the strain in one of the resistors as a function of the pressure on the diaphragm, let L be the length of the side of the square diaphragm and H be its thickness. Following [23], the normal displacement $\hat{w}$ of the diaphragm as a function of its horizontal x and y coordinates is approximated as a function of the form

$$\hat{w}(x,y) = \frac{c_1}{4}\left[1 + \cos\left(\frac{2\pi x}{L}\right)\right]\left[1 + \cos\left(\frac{2\pi y}{L}\right)\right], \quad (5)$$

where the origin is the center of the plate and c_1[1] is the deflection at the center of the diaphragm. The resulting pressure-deflection relation is

$$P = \frac{\pi^4 E H^3}{6(1-\nu^2)L^4} c_1, \quad (6)$$

[1]The subscript in c_1 refers to the fact that it is the amplitude of the first mode of vibration for the diaphragm. This paper does not discuss other modes, but the notation is used for consistency with other works.

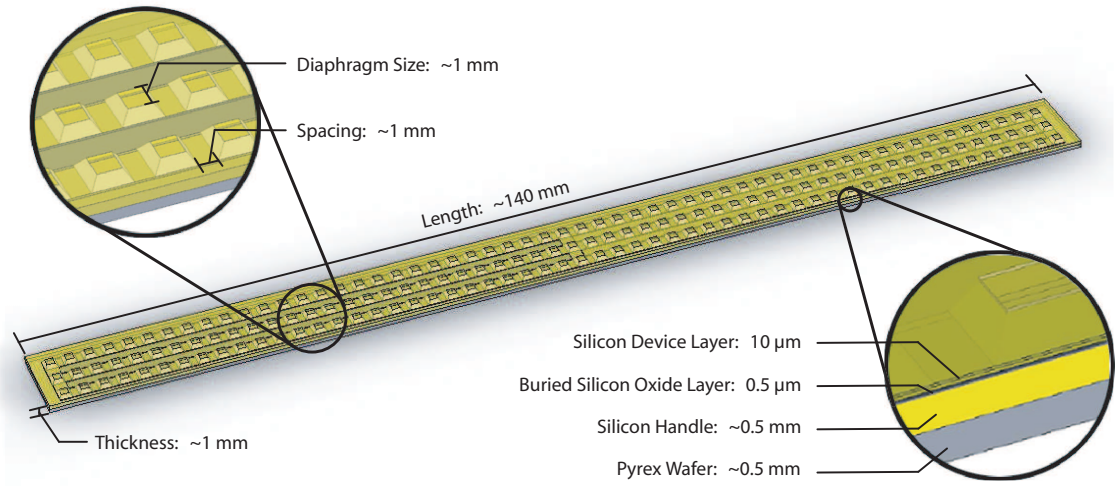

Figure 14: Diagram of pressure-sensor array with basic structure depicted.

where P is the pressure difference across the diaphragm, E and ν are the Young's modulus and the Poisson's ratio for the diaphragm, respectively. As calculated in [24] using finite-element methods, the stress in the x-direction is

$$\sigma_x = 0.294 \left(\frac{L}{H}\right)^2 P, . \tag{7}$$

Given $L = 2000\,\mu\text{m}$ and $H = 20\,\mu\text{m}$ as typical membrane sizes, the stress is

$$\sigma_x = 2940 \cdot P. \tag{8}$$

As shown in [25], the strain in the x direction is

$$\begin{aligned} \epsilon_x &= K \left(\frac{L}{H}\right)^2 \left(\frac{P}{E}\right) \left(\frac{z}{H}\right) \left[\cos\left(\frac{2\pi x}{L}\right)\right] \\ &\cdot \left[1 + \cos\left(\frac{2\pi y}{L}\right)\right], \end{aligned} \tag{9}$$

where z is the vertical position within the membrane relative to the center plane, and it can be shown that the relative change in resistance for a resistor segment deformed by being bonded to the top of such a plate is

$$\frac{\Delta R}{R} \approx \frac{1}{1-\nu}\epsilon_l + \frac{2\nu - 1}{1-\nu}\epsilon_w, \tag{10}$$

where ϵ_l and ϵ_w are the strains along the resistor length and width, respectively.

3.3 Deflection and Sensitivity

The maximum deflection c_1 of the diaphragm, which occurs at the center, is

$$c_1 = \frac{K}{\pi^2} \left(\frac{P}{E}\right) \left(\frac{L^4}{H^3}\right). \tag{11}$$

The maximum strain in the x direction, which also occurs at the center, is

$$\epsilon_x = 2K \left(\frac{L}{H}\right)^2 \left(\frac{P}{E}\right) \left(\frac{z}{H}\right). \tag{12}$$

By symmetry, the strain the y direction is the same. For $K = 0.294$, $E = 47\,\text{GPa}$ (silicon), $L = 2000\,\mu\text{m}$, and $H = 20\mu\text{m}$, these quantities become

$$\frac{\epsilon_i}{P} = 1.25 \times 10^{-7}\,\text{Pa}^{-1} \tag{13}$$

$$\frac{c_1}{P} = 1.3\,\text{nm/Pa}. \tag{14}$$

Substituting the value given in Equation 13 into Equation 10 produces the relative change in resistance:

$$\frac{\Delta R}{R} \approx \left(1.07 \times 10^{-7}\,\text{Pa}^{-1}\right) \cdot P. \tag{15}$$

Thus, for a typical source voltage of $V_s = 10\,\text{V}$ for the Wheatstone bridge, the sensitivity of a strain-gauge resistor sensor located at the center of the diaphragm is on the order of $1\,\mu\text{V/Pa}$.

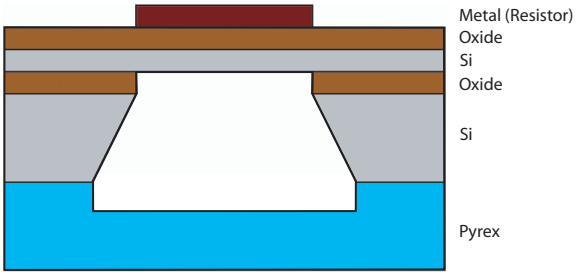

Figure 15: Sideview of the fabrication layers of a single sensor (not to scale). The portion of the silicon and oxide layers above the etched hole is the diaphragm.

3.4 Noise

Thermal noise voltage is on the order of

$$V_N = \sqrt{4kTRf}, \tag{16}$$

where k is Boltzmann's constant, T is temperature, R is resistance, and f is the filtered bandwidth of the electrical signal [23]. Thus, for $T = 300\,\mathrm{K}$, $R = 10\,\mathrm{k}\Omega$, and $f = 3\,\mathrm{kHz}$, the thermal noise voltage is 0.7 μV.

Therefore, the pressure sensitivity of the sensors is on the order of 1 Pa for a 10 V source, which is the level needed for the aforementioned applications.

3.5 Fabrication

The fabrication of a basic pressure sensor array is described here. The steps were performed in the MIT Microsystems Technology Laboratories and can be done with standard CMOS/MEMS processes.

A double-side polished silicon-on-insulator (SOI) wafer, which contains a 20 μm thick Si layer to be used as the diaphragm, is first masked with a silicon-nitride (Si_3N_4) layer. The nitride is removed from the device (diaphragm) side, oxide is grown on the bare silicon to act as an insulating layer, and the metal resistors are deposited on the oxide. The back side of the SOI wafer is then etched using potassium-hydroxide (KOH) with the nitride as a mask and the original SOI oxide as an etch stop to form an air cavity. The remaining Si_3N_4 mask is then dry etched away to expose silicon. In the meantime, a Pyrex glass wafer is laser etched to create shallow valleys that allow air to pass. The Pyrex and SOI wafers are then anodically bonded to form arrays of the devices shows in Figure 15.

4 Conclusion

Experiments have been described which demonstrate that it is possible to distinguish details in the shape of objects underwater using an array of passive pressure sensors under conditions similar to those encountered by fish and man-made vehicles. Two methods were presented for discriminating between cylindrical moving stimuli of square or round cross sections of different sizes. Both methods successfully classified the shape of the cross section, though the hand-picked features had a considerably higher failure rate (9.8%) than the principal components (1.2%). When considering the broader picture however, the intuitively chosen features may be more flexible than the principal components. Although fish have demonstrated the ability to discriminate between similar stimuli, their method of discrimination is not yet known.

The classification of stimuli shape was possible in a range of conditions. The velocities, sizes, and separation distances tested did not hinder the ability to classify the cross sections. There is no claim made that the results will work for all velocities, sizes, or separations, but it is evident that within a range of the tested conditions it is possible to discriminate between the two shapes.

The pressure time series from the experiments were taken to be representative of the spatial pressure distributions that might occur on a fish or sensor array. This assumption relied on the constant velocity of the stimuli. Certain aspects of the pressure traces, particularly those corresponding to the unsteady wake region behind the moving object, may not be accurate in this respect. Further tests, in particular with a full dense pressure sensor array, need to be performed to explore this further. In addition, more information maybe be available for discriminating between moving objects when multiple sensors are considered as a group. For example, the relative velocity of the object can be easily calculated (though it was not used in these analyses).

Considering the data for cylindrical shapes with two cross sections, basic specifications for the performance of the MEMS pressure sensor array were extracted. These specifications determined the maximum spacing and minimum sensitivity of the device. It was also demonstrated that the proposed pressure sensor system, which can be manufactured with standard MEMS techniques, can achieve a pressure resolution on the order of 1 Pa, thus meeting the required pressure resolution.

References

[1] J. C. Montgomery, S. Coombs, and C. F. Baker. The mechanosensory lateral line system of the hypogean form of *Astyanax fasciatus*. *Evolutionary Biology of Fishes*, 62:87–96, 2001.

[2] C. von Campenhausen, I. Riess, and R. Weissert. Detection of stationary objects by the blind cave fish *Anoptichthys jordani* (Characidae). *Journal of Comparative Physiology*, 143:369–374, 1981.

[3] K. Pohlmann, J. Atema, and T. Breithaupt. The importance of the lateral line in nocturnal predation of piscivorous catfish. *Journal of Experimental Biology*, 207:2971–2978, 2004.

[4] M. A. Gibbs. Lateral line receptors: Where do they come from developmentally and where is our research going? *Brain, Behavior, and Evolution*, 64: 163–181, 2004.

[5] S. Coombs. Smart skins: Information processing by lateral line flow sensors. *Autonomous Robotics*, 11:255–261, 2001.

[6] S. M. van Netten. Hydrodynamic detection by cupulae in a lateral line canal: Functional relations between physics and physiology. *Biological Cybernetics*, 94:67–85, 2006.

[7] C. B. Braun and S. Coombs. The overlapping roles of the inner ear and lateral line: the active space of dipole source detection. *Philosophical Transactions of the Royal Society of London*, 355:1115–1119, 2000.

[8] G. G. Harris and W. A. van Bergeijk. Evidence that the lateral line organ responds to near field displacements of sound sources in water. *Journal of Acoustical Society of America*, 34:1831–1841, 1962.

[9] S. Coombs, M. Hastings, and J. J. Finneran. Modeling and measuring lateral line excitation patterns to changing dipole source locations. *Journal of Comparative Physiology A*, 178:359–371, 1996.

[10] S. Coombs and R. R. Fay. Dipole source localization by mottled sculpin, *Cottus bairdi*. *Journal of the Acoustical Society of America*, 93:2116–2123, 1993.

[11] Y. Yang, J. Chen, J. Engel, S. Pandya, N. Chen, C. Tucker, S. Coombs, and C. Liu. Distant touch hydrodynamic imaging with an artificial lateral line. *Proceedings of the National Academy of Science*, 103(50):18891–18895, December 2006.

[12] H. Bleckmann, I. Waldner, and E. Schwartz. Frequency discrimination of the surface-feeding fish *Aplocheilus lineatus* - a prerequisite for prey localization? *Journal of Comparative Physiology A*, 143:485–490, 1981.

[13] R. Weissert and C. von Campenhausen. Discrimination between stationary objects by the blind cave fish *Anoptichthys jordani* (characidae). *Journal of Comparative Physiology A*, 143:375–381, 1981.

[14] E. S. Hassan. On the discrimination of spatial intervals by the blind cave fish (*Anoptichthys jordani*). *Journal of Comparative Physiology A*, 159:701–710, 1986.

[15] T. Teyke. Collision with and avoidance of obstacles by blind cave fish *Anoptichthys jordani* (characidae). *Journal of Comparative Physiology A*, 157: 837–843, 1985.

[16] E. S. Hassan. Mathematical description of the stimuli to the lateral line system of fish derived from a 3-dimensional field analysis: I. the cases of moving in open water and of gliding towards a plane surface. *Biological Cybernetics*, 66:443–452, 1992.

[17] E. S. Hassan. Mathematical description of the stimuli to the lateral line system of fish derived from a 3-dimensional field analysis: II. the case of gliding alongside or above a plane surface. *Biological Cybernetics*, 66:453–461, 1992.

[18] D. Vogel and H. Bleckmann. Behavioral discrimination of water motions caused by moving objects. *Journal of Comparative Physiology A*, 186:1107–1117, 2000.

[19] J. N. Newman. *Marine Hydrodynamics*. MIT Press, Cambridge, Massachusetts, 1977.

[20] S. Theodoridis and K. Koutroumbas. *Pattern Recognition*. Academic Press, San Diego, California, third edition, 2006.

[21] I. T. Jolliffe. *Principal Component Analysis*. Springer, New York, New York, second edition, 2002.

[22] J. E. Jackson. *A User's Guide to Principal Components*. Wiley, Hoboken, New Jersey, 2003.

[23] S. D. Senturia. *Microsystem Design*. Kluwer Academic Publishers, Boston, Massachusetts, 2001.

[24] S. K. Clark and K. D. Wise. Pressure sensitivity in anisotropically etched thin-diaphragm pressure sensors. *IEEE Transactions on Electronic Devices*, 26(12):1887–1896, December 1979.

[25] S. Timoshenko. *Theory of Plates and Shells*. McGraw-Hill Book Company, Inc., New York, New York, second edition, 1959.

[26] M. Ozgoren. Flow structure in the downstream of square and circular cylinders. *Flow Measurements and Instrumentation*, 17:225–235, 2005.

[27] T. Suzuki and T. Colonius. Inverse-imaging method for detection of a vortex in a channel. *American Institute of Aeronautics and Astronautics Journal*, 41:1743–1751, 2003.